applied sciences

MDPI

Article

Selecting Optimal Long Short-Term Memory (LSTM) Architectures for Online Estimation of Mean Arterial Pressure (MAP) in Patients Undergoing General Anesthesia

Ghada Ben Othman [1,*], Dana Copot [1], Erhan Yumuk [1], Martine Neckebroek [2] and Clara M. Ionescu [1]

[1] Research Group on Dynamical Systems and Control, Department of Electromechanics, Systems and Metal Engineering, Ghent University, Tech Lane Science Park 125, 9052 Ghent, Belgium; dana.copot@ugent.be (D.C.); erhan.yumuk@ugent.be (E.Y.); claramihaela.ionescu@ugent.be (C.M.I.)
[2] Department of Anesthesia, Ghent University Hospital, Corneel Heymanslaan 10, 9000 Ghent, Belgium; martine.neckebroek@ugent.be
* Correspondence: ghada.benothman@ugent.be

Abstract: In the realm of anesthetic management during surgical procedures, the reliable estimation of mean arterial pressure (MAP) is critical for ensuring patient safety and optimizing drug administration. This paper investigates the determination of the optimal Long Short-Term Memory (LSTM) architectures aimed at enhancing the estimation of MAP. Using data from a trial involving 70 patients undergoing Total Intravenous Anesthesia (TIVA) provides the effect-site concentrations of Propofol and Remifentanil as key input variables for LSTM models. Our solution categorizes the selection strategies into three distinct methodologies: (i) a population-based method applying a single model across all patients, (ii) a patient-specific method tailoring models to individual physiological responses, and (iii) a novel category-specific method that groups patients based on the correlation between input variables, the effect-site concentrations of Propofol and Remifentanil, and MAP output. The novelty of this paper lies in the proposed method to identify the optimal architecture, evaluating 288 models to fine-tune the best model for each patient and category. Our findings suggest that the patient-specific model outperforms others, highlighting the benefits of personalized model architectures in medical artificial intelligence (AI) applications. The category-specific models provide a pragmatic solution, with reasonable accuracy and enhanced computational efficiency. By contrast, the population-based models, while efficient, have a lower estimation accuracy. This study confirms the significance of sophisticated LSTM architectures in medical AI, providing insights into their potential for advancing patient-specific anesthetic care by accurately online estimating MAP.

Keywords: artificial intelligence; anesthesia; LSTM; data-driven LSTM architecture; online estimation; hemodynamics

Citation: Ben Othman, G.; Copot, D.; Yumuk, E.; Neckebroek, M.; Ionescu, C.M. Selecting Optimal Long Short-Term Memory (LSTM) Architectures for Online Estimation of Mean Arterial Pressure (MAP) in Patients Undergoing General Anesthesia. *Appl. Sci.* **2024**, *14*, 5556. https://doi.org/10.3390/app14135556

Academic Editor: Lei Zhang

Received: 28 May 2024
Revised: 20 June 2024
Accepted: 21 June 2024
Published: 26 June 2024

1. Introduction

During surgical procedures, as patients undergo anesthesia, the administration of Remifentanil and Propofol stands as a cornerstone, actively shaping the patient's physiological responses. These pharmacologically distinct agents, an opioid analgesic and a hypnotic, contribute to achieving and maintaining an optimal level of anesthesia. However, beyond their primary hypnotic and analgesic roles, these drugs may exert side effects, potentially influencing the physiological response of the patient, specifically the mean arterial pressure (MAP) [1]. MAP serves as a vital indicator of perfusion and oxygen delivery to organs, making its accurate prediction during surgery imperative [2]. The challenge at hand is not only to comprehend the dynamics of how Remifentanil and Propofol influence MAP but also to devise an online predictive framework that balances the need for accuracy with computational efficiency.

Artificial intelligence (AI) has revolutionized various aspects of the medical field, offering advanced solutions for diagnostics, treatment planning, and patient management [3,4]. In the domain of AI applications in anesthesia, the complex interplay between drug administration and patient physiological responses has been a focal point of exploration [5]. Understanding this dynamic interaction is crucial for optimizing patient outcomes.

There exists a relationship between the architectural design of neural network models and their predictive performance [6]. LSTM architecture selection for predicting physiological parameters has received notable attention [7] because of its proficiency in capturing temporal dependencies within the data [8,9]. LSTM networks have been increasingly applied in the prediction of medical signals due to their ability to model time series data effectively. Particularly in the context of irregularly sampled medical time series, which is common in healthcare data [10], LSTMs demonstrate notable advantages. These networks adeptly handle intra-series irregularities (varying time intervals within a single data stream) and inter-series irregularities (different sampling rates across multiple data streams) [11,12]. This capability is crucial for modeling complex medical signals, e.g., blood pressure, where data points might be unevenly spaced in time. Further, the integration of LSTMs with other neural network architectures, like Convolutional Neural Networks (CNNs), has shown promising results in the medical field. Specifically for anesthesia, using inputs like Propofol and Remifentanil to predict MAP, the ability of LSTM to capture temporal dependencies and handle missing or irregular data points makes it a suitable choice. The ability of LSTM to process time-dependent data and handle variations in data sampling rates are key reasons for their suitability in estimating MAP under anesthesia. The choice of the best architecture for LSTM models has often been driven either by tests involving multiple architectures, or by the background expertise of researchers [13,14]. The following question arises: is the selected LSTM architecture truly the optimal choice for a given AI application, or is there an optimal criterion that demands consideration, e.g., the computational time?

We recognize the need to build more optimal architectures for deep learning models, with enhanced accuracy and computational efficiency, since we aim to obtain an online MAP estimation solution. In this context, our paper addresses this dual imperative by introducing three distinct selection approaches of the LSTM architecture. The first method involves a population-based architecture, considering 70 patients under anesthesia. The second method adopts a patient-specific strategy, building an LSTM architecture uniquely for each patient. The third method employs a novel categorization method based on input–output correlation, wherein patients are categorized according to the correlation of inputs (effect-site concentration of Propofol CeProp (μg/mL) and effect-site concentration of Remifentanil CeRemi (ng/mL)) with the output MAP (mmHg), and a specific architecture is identified for each category.

Central to our study is to investigate the possible balance between computational efficiency and estimation accuracy across these diverse methodologies. This study introduces a novel method that compares 288 different architectures to determine the optimal model for each patient and category. All 70 patients were subject to routine monitoring during TIVA, and they were sedated using Propofol. Additionally, Remifentanil was administered through target-controlled infusion (TCI) to manage supplementary analgesia. We calculated CeProp (the effect site concentration of Propofol) and CeRemi (the effect site concentration of Remifentanil), using the Schnider and Minto pharmacokinetic models, respectively [15,16]. Through this multifaceted approach, we simultaneously enhance accuracy, computational efficiency, and the applicability of LSTM models in the context of physiological parameter prediction in anesthesia.

This paper is organized as follows: Section 2 presents the description of the clinical trial protocol. Section 2 also provides an in-depth exploration of the methodology, focusing on the regression employing LSTM networks and the critical parameters influencing the performance of the model. Section 3 presents the results obtained from three distinct methods, population-specific, patient-specific, and category-specific, comparing their performance based on key metrics. The discussion in Section 4 critically examines the implications of our

findings, the novelty of the paper, and its limitations. Finally, Section 5 offers concluding remarks and highlights the future aspects of research in this field.

2. Methodology

2.1. Clinical Trial Protocol

The patients used in this study, scheduled for elective surgery under Total Intravenous Anesthesia (TIVA), were selected based on inclusion criteria like ages 18–80 years, American Society of Anesthesiologists (ASA) Class I, II, and III, and the ability to provide informed consent. Exclusion criteria included patients with chronic pain, pregnant women, and those with electrically sensitive devices. This study adhered to ISO 14155 standards [17] for good clinical practice and complied with European Regulation (EU) 2017/745 [18]. Ethical approval was obtained, and informed consent was provided by all participants. During anesthesia, Propofol and Remifentanil were administered using target-controlled infusion (TCI) with initial target concentrations set at 5 µg/mL for Propofol and 3 ng/mL for Remifentanil. Dosages were adjusted by anesthesiologists based on heart rate and blood pressure. Muscle relaxation was achieved using rocuronium, guided by an induction dose of 0.3 mg/kg and further boluses as needed. MAP was monitored in mmHg using a hemodynamics monitor (GE HealthCare, Chicago, IL, USA). The primary objective outcome of this clinical study has been published in [19]. The biometrics of the 70 patients are detailed in Appendix B, and the variability in MAP among these patients is discussed in Appendix C.

2.2. Model Design and Architecture

The computational unit used for calculations in this study was a Dell workstation equipped with an Intel® Xeon® Bronze 3204 CPU @ 1.90 GHz, 64 GB of RAM, running Windows 11 Pro for Workstations. The software environment used for data processing and analysis was MATLAB v.2022.

In the context of regression employing LSTM networks, the architecture primarily comprises a sequence input layer and an LSTM layer with a specified number of hidden units [20,21]. In this work, the inputs to the LSTM model are the effect site concentrations CeProp and CeRemi. The LSTM layer is followed by a Fully Connected Layer and a Regression Layer. Notably, the desired output of this architecture is the MAP [22]. The selection of parameters in an LSTM network plays a pivotal role in determining its performance for regression tasks. These parameters, as summarized in Table 1, encompass various aspects, e.g., the number of LSTM layers, neurons per layer, activation functions, number of epochs, optimizer choice, and mini-batch size.

Table 1. Description of LSTM Parameters.

Parameter	Role	MATLAB Code Example
LSTM layers	Determines the depth of the neural network.	`layers = [lstmLayer(16), lstmLayer(32), ...]`
Neurons per layer	Defines the number of basic processing units in each LSTM layer.	`neurons = [16, 64];`
State activation function	Activation function for updating the cell and hidden state in the LSTM layer.	`stateActivation = {tanh, softsign};`
Gate activation function	Activation function for the gates in the LSTM layer.	`gateActivation = {sigmoid, hard-sigmoid};`
Number of epochs	Controls the number of training iterations through the entire dataset.	`epochs = [50, 100, 200, ...];`
Optimizer	Adjusts model parameters during training to minimize the error.	`optimizer = {adam, rmsprop, sgd, ...};`
Mini-batch size	Determines the number of training examples used in each update.	`miniBatchSize = [16, 32, 64];`

The number of LSTM layers and neurons per layer defines the complexity of the network, with a careful balance needed to avoid overfitting. Activation functions play a pivotal role in how information is stored and flows through the LSTM.

For the `StateActivationFunction`, common choices include `tanh` and `softsign`. The hyperbolic tangent function `tanh` is defined as follows :

$$\tanh(x) = \frac{e^{2x} - 1}{e^{2x} + 1}, \tag{1}$$

while the softsign function is defined as:

$$\texttt{softsign}(x) = \frac{x}{1 + |x|}. \tag{2}$$

These functions impact the ability of the network to capture long-term dependencies and update the cell and hidden state [23]. The LSTM architecture is detailed in Appendix A.

For the `GateActivationFunction`, common choices are `sigmoid` and `hard-sigmoid`. The sigmoid function is defined as follows:

$$\sigma(x) = \frac{1}{1 + e^{-x}}, \tag{3}$$

and the hard sigmoid function is defined as follows:

$$\sigma(x) = \begin{cases} 0 & \text{if } x < -2.5, \\ 0.2x + 0.5 & \text{if } -2.5 \leq x \leq 2.5. \\ 1 & \text{if } x > 2.5 \end{cases} \tag{4}$$

These functions are applied to the gates in the LSTM layer, influencing how information flows through the network [24].

Optimizers, e.g., `adam`, `rmsprop`, and `sgd` (stochastic gradient descent), also play a key role in adjusting model parameters during training. The `adam` optimizer dynamically adapts learning rates using moment estimates, enhancing convergence speed. Its updated equations are

$$m_t = \beta_1 \cdot m_{t-1} + (1 - \beta_1) \cdot g_t, \tag{5}$$

$$v_t = \beta_2 \cdot v_{t-1} + (1 - \beta_2) \cdot g_t^2, \tag{6}$$

$$\theta_t = \theta_{t-1} - \alpha \cdot \frac{m_t}{\sqrt{v_t} + \epsilon} \tag{7}$$

where θ represents the model parameters, g_t is the gradient at time step t, m_t and v_t are the first and second moment estimates, respectively (which are weighted averages of past gradients), β_1 and β_2 are exponential decay rates for moment estimates, α is the learning rate, and ϵ is a small constant (typically 10^{-8}) to prevent division by zero, ensuring numerical stability. The command `rmsprop` uses a moving average of squared gradients, and `sgd` employs the standard stochastic gradient descent update rule. The choice of optimizer depends on factors like the specific characteristics of the dataset and the desired training efficiency [25].

The depth and width of the network, activation functions, number of epochs, optimizer choice, and mini-batch size collectively impact the ability of the model to capture patterns and its training efficiency [14]. These parameters not only influence accuracy but also significantly impact the training time. In this work, three methods for choosing LSTM architectures are proposed: population-specific, patient-specific, and category-specific.

2.3. Performance Metrics

To assess the performance of the estimation results obtained from the methods (population-specific, patient-specific, and category-specific), the following performance metrics are employed:

(i) Mean Squared Error (MSE): MSE measures the average squared difference between the actual y_i and predicted $\hat{y}_i$ values and is calculated as

$$\text{MSE} = \frac{1}{n}\sum_{i=1}^{n}(y_i - \hat{y}_i)^2. \tag{8}$$

(ii) Mean Absolute Error (MAE): MAE computes the average absolute difference between the predicted and actual values, providing a more interpretable measure:

$$\text{MAE} = \frac{1}{n}\sum_{i=1}^{n}|y_i - \hat{y}_i|. \tag{9}$$

(iii) Coefficient of Determination ($\boldsymbol{R^2}$):R^2 quantifies the proportion of the variance in the dependent variable that is predictable from the independent variable(s), and is given by

$$R^2 = 1 - \frac{\sum_{i=1}^{n}(y_i - \hat{y}_i)^2}{\sum_{i=1}^{n}(y_i - \bar{y})^2}, \tag{10}$$

where $\bar{y}$ is the mean value of the observed values.

The MSE and MAE provide insights into the accuracy of estimations, with lower values indicating better performance. R^2 ranges from 0 to 1, where a higher R^2 signifies a better fit of the model to the data. The results obtained from the three methods are compared in terms of estimation accuracy and computational efficiency. The analysis encompasses MSE, MAE, and R^2 values to assess the effectiveness of each method. Additionally, consideration is given to the time consumed by each method in finding the optimal architecture, aiming to identify the most efficient method.

2.4. Population-Specific Method

This method uses one user-defined LSTM architecture for 70 patients. The architecture presented in Figure 1 is the result of an iterative process where a few different architectures are tested. The selection of this specific architecture follows the traditional approach, relying on the expertise of the practitioner [26]. The choice is based on the ability of the architecture to achieve acceptable MSE results and its capacity to capture complex temporal dependencies in the time series data of CeProp and CeRemi.

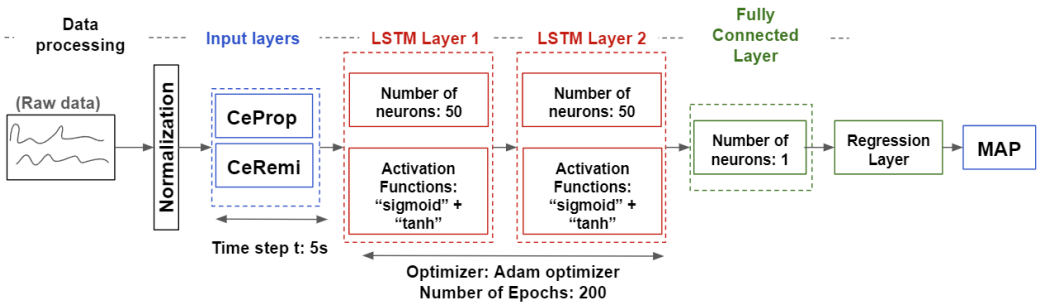

Figure 1. The architecture of the LSTM-based regression model for the population-specific method.

The input layer includes CeProp and CeRemi values, which are processed offline and provided to the model simultaneously as the training data. The LSTM layers process these inputs over a sampling time of 5 s. The normalization step is applied to ensure consistent scaling across signals, for stable training. The architecture consists of two LSTM layers, each

with 50 neurons. This decision balances model complexity with computational efficiency, allowing the model to effectively capture and learn from the temporal patterns present in the data. The activation functions in both LSTM layers are set to the default values in MATLAB R2022a, which are `sigmoid` for gate activation and hyperbolic tangent `tanh` for state activation.

The Fully Connected Layer is employed to consolidate information from the LSTM layers before passing it through the Regression Layer. This design facilitates the extraction of high-level features from the LSTM layers and prepares the model for the final regression task. The `adam` optimizer is employed with a set number of epochs (200) to optimize the model parameters. The Adam optimizer is known for its efficiency in handling sparse gradients and adapting learning rates during training, making it a suitable candidate for this regression task. The *Deep Learning* Toolbox in MATLAB® from MathWorks® version 14.1. was used for the implementation of the LSTM network, including the layers (`sequenceInputLayer`, `lstmLayer`, `fullyConnectedLayer`, `regressionLayer`) and training functions (`trainNetwork`, `predict`) [27].

2.5. Patient-Specific Method

To enhance personalized medicine, this novel method identifies the optimal architecture for the LSTM model for each patient. The methodology explores various configurations of LSTM architectures for each patient through an iterative process. The patient-specific selection process is illustrated in Algorithm 1, summarizing the steps necessary to identify the best LSTM architecture for each of the 70 patients.

Algorithm 1 Best LSTM architecture search

```
1:  Initialize bestMSE = ∞
2:  Define numLayers = [2, 3]
3:  Define numNeurons = [10, 50, 75, 100]
4:  Define optimizers = {'adam', 'sgdm', 'rmsprop'}
5:  Define stateActivations = {'tanh', 'softsign'}
6:  Define gateActivations = {'hard-sigmoid', 'sigmoid'}
7:  Define minibatchSizes = [16, 32, 64]
8:  for numLayer in numLayers do
9:      for numNeuron in numNeurons do
10:         for optimizer in optimizers do
11:             for stateActivation in stateActivations do
12:                 for gateActivation in gateActivations do
13:                     for minibatchSize in minibatchSizes do
14:                         Build and train LSTM model with current hyperparameters
15:                         Evaluate model performance and calculate MSE
16:                         if MSE <bestMSE then
17:                             bestMSE = MSE
18:                             bestModel = current model architecture
19:                         end if
20:                     end for
21:                 end for
22:             end for
23:         end for
24:     end for
25: end for
26: Output bestModel and bestMSE
```

The algorithm execution consists of the following loops: The loop on line 8 varies the number of LSTM layers, and the number of LSTM layers is set between 2 and 3 to prevent overfitting or underfitting of the model; the loop on line 9 adjusts the number of neurons within each layer; the loop on line 10 explores different optimizers, including `adam`, `sgdm`,

and rmsprop; the loops on (lines 11 and 12 iterate over activation functions for the state and gate, respectively; the loop on line 13 varies the mini-batch sizes. Within each run of the loops, a model is built, trained, and evaluated by calculating the MSE. If the MSE of the current model is lower than the best MSE recorded so far, the model architecture is updated to the new best. The design of the loops reflects an intensive strategy, enabling the algorithm to evaluate a wide range of architectural configurations. This algorithm is optimum seeking but is computationally intensive, requiring 130 h and 20160 iterations to identify the best architecture for each of the 70 patients.

2.6. Category-Specific Method

To tackle the computational intensity inherent of the patient-specific method, we propose a novel category-specific method based on the mean correlation between inputs (CeProp/CeRemi) and the output (MAP). The reasoning for developing a category-specific method is based on the significant impact of correlation rates between inputs and outputs on estimation accuracy. This leads to an increased complexity of neural network architectures [28,29]. The mean correlation is computed for pairs (CeProp/MAP and CeRemi/MAP), and the resulting values are categorized into five distinct ranges. Each category represents a specific range, providing insights into the relationship between inputs and output.

The correlations between CeProp, CeRemi, and MAP are calculated as follows:

$$\text{Corr}(CeProp, MAP) = \frac{\sum_{i=1}^{n}(CeProp_i - \overline{CeProp})(MAP_i - \overline{MAP})}{\sqrt{\sum_{i=1}^{n}(CeProp_i - \overline{CeProp})^2 \sum_{i=1}^{n}(MAP_i - \overline{MAP})^2}}, \quad (11)$$

$$\text{Corr}(CeRemi, MAP) = \frac{\sum_{i=1}^{n}(CeRemi_i - \overline{CeRemi})(MAP_i - \overline{MAP})}{\sqrt{\sum_{i=1}^{n}(CeRemi_i - \overline{CeRemi})^2 \sum_{i=1}^{n}(MAP_i - \overline{MAP})^2}} \quad (12)$$

where n is the number of samples, and $CeProp_i$, $CeRemi_i$, and MAP_i represent the data points for CeProp, CeRemi, and MAP at the i-th time point, respectively. $\overline{CeProp}$, $\overline{CeRemi}$, and $\overline{MAP}$ represent the means of the corresponding sets. The obtained mean correlation value is classified into the appropriate range as given in Table 2.

Table 2. Correlation groups and patients.

Categories	Correlation Range	Patients
1 Weak or no correlation	0 to 0.10	Patient 15
2 Weak correlation	0.10 to 0.20	Patient 59
3 Mild correlation	0.20 to 0.40	Patients 10, 28, 30, 52, 60, 62, 65, 68
4 Moderate correlation	0.40 to 0.70	Patients 2, 4, 6, 12, 13, 19, 20, 21, 23, 26, 27, 29, 31, 32, 33, 34, 37, 40, 41, 42, 44, 45, 46, 47, 49, 50, 51, 53, 55, 57, 58, 61, 67, 69
5 Strong correlation	0.70 to 1.00	Patient 1, 3, 5, 7, 8, 9, 11, 14, 16, 17, 18, 22, 24, 25, 35, 36, 38, 39, 43, 48, 54, 56, 63, 64, 66, 70

In contrast with the patient-specific method, within the category-specific method, Algorithm 1 is executed 5 times only instead of 70. Consequently, at the conclusion of this process, we obtain one distinct architecture for every correlation category. This method significantly reduces the total number of iterations (1440) compared to the examination of all 70 patients.

3. Results

The dataset was split into 70% for training and 30% for testing, and the number of epochs for the LSTM architecture was set at 200.

3.1. Population-Specific Method Results

The architecture used in the population-specific method consists of two LSTM layers with 50 neurons each, using sigmoid for gate activation and hyperbolic tangent tanh for state activation, followed by a Fully Connected Layer and a Regression Layer, optimized using the Adam optimizer. Figure 2 shows the comparison between LSTM-estimated MAP versus real MAP values for three patients with worst fitting (Figure 2a), average fitting (Figure 2b) and best fitting (Figure 2c).

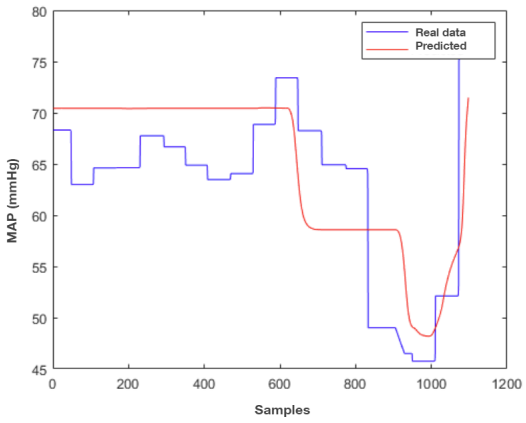

(**a**) Patient 15

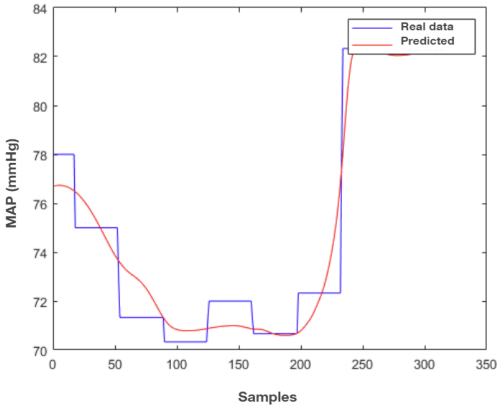

(**b**) Patient 28

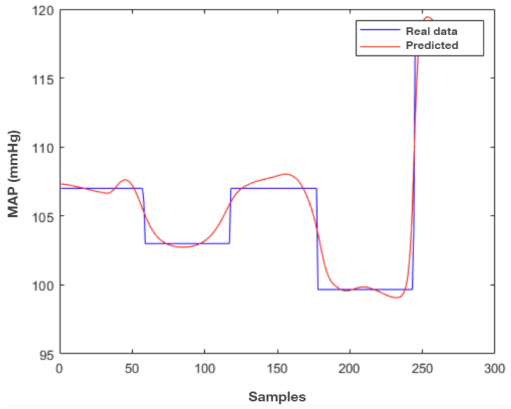

(**c**) Patient 63

Figure 2. Results of LSTM-estimated MAP vs. actual MAP values for different patients using the population-specific method.

For Patient 15 (Figure 2a), the LSTM model fails to predict MAP accurately, resulting in a modest R^2 value of 0.38, due to the weak correlation between inputs (CeProp, CeRemi) and output (MAP) (Table 2). As depicted in Figure 2a, similarly, Patient 28 (Figure 2b) shows a less accurate estimation with an R^2 value of 0.58. By contrast, Patient 63 (Figure 2c) shows an accurate estimated MAP profile with an R^2 value of 0.7. The strong correlation between drug concentrations and MAP enhances the ability of the model to accurately capture and predict MAP dynamics.

3.2. Patient-Specific Method Results

The results of the new algorithm presented in Algorithm 1 for the patient-specific method are depicted in Figure 3.

For the state activation function (Figure 3a), `tanh` dominates with an appearance in 83% of patients, while `softsign` is the best state activation function for 17% of patients. The results of the gate activation function (Figure 3b) show that the `sigmoid` is the most frequent, with an appearance in 67.1% of patients. This result suggests that the `sigmoid` activation function is more adept at regulating the flow of information through the LSTM gates, potentially contributing to better model convergence. The results in (Figure 3c) reveal that the `adam` optimizer is the most prevalent optimizer with presence in 95.7% of patients. By contrast, `rmsprop` was identified in only three patients. The mini-batch size of 32 is the most prevalent (Figure 3d), occurring in 41% of the patients. The selection of 100 neurons per layer (Figure 3e) is the predominant configuration, appearing in 46% of patients, with variations in other configurations (50 neurons at 20%, 75 neurons at 27%, 10 neurons at 7%). The results (Figure 3f) indicate that 67% of patients fall within the three-layer approach. The variations across parameters emphasize the need for personalized adjustments. This analysis enhances our understanding of prevalent trends and informs future refinements in LSTM architecture selection for physiological parameter estimation during anesthesia.

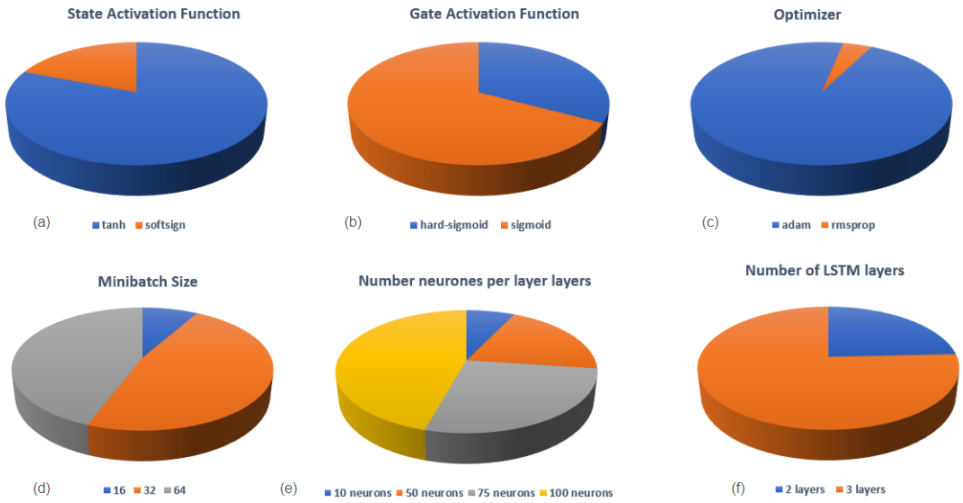

Figure 3. Percentages of appearance of each option among the different iterations and loops for the patient-specific method.

The best architecture for each patient is used to estimate the MAP. The results of patients with the worst and best fitting estimations are presented in Figures 4a and 4b, respectively. The accuracy of the fitting is higher when the correlation between inputs (CeProp, CeRemi) and output (MAP) is strong, as seen in Patient 63. Conversely, for Patient 15, the estimation accuracy is lower due to the weak correlation between inputs and output.

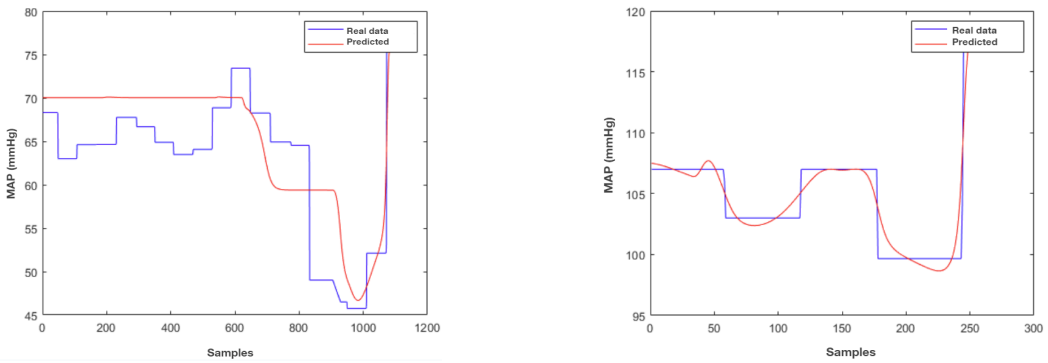

(**a**) Patient 15 (**b**) Patient 63

Figure 4. Results of LSTM-estimated MAP vs. actual MAP values for different patients using the patient-specific method.

3.3. Category-Specific Method Results

In Figure 5, the LSTM-estimated MAP and measured MAP for one patient per category are shown. Figure 5a, 5b, and 5c show the results obtained for patients in categories 1, 2, and 3, respectively. Variations in estimation accuracy can be observed, specifically for Patient 15 (weak or no correlation category) and Patient 59 (weak correlation category); the results demonstrate a significant difference between estimated and real MAP values. This highlights the failure of this method for accurate estimation in weak correlation situations. For patient 28 (mild correlation category), the results show good estimation. This emphasizes the impact of correlation strength on predictive accuracy, as milder correlations present additional challenges in capturing the dynamics of physiological responses.

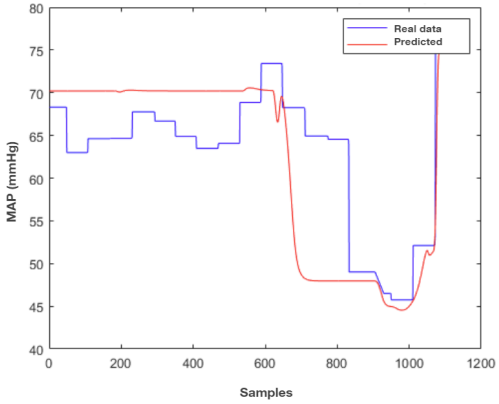

(**a**) Patient 15—Category 1

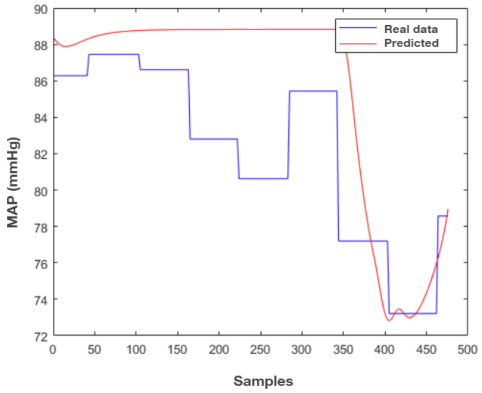

(**b**) Patient 59—Category 2

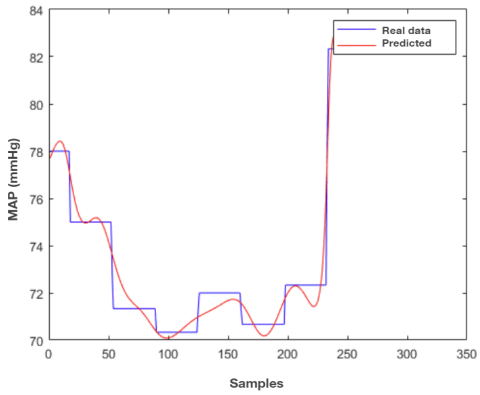

(**c**) Patient 28—Category 3

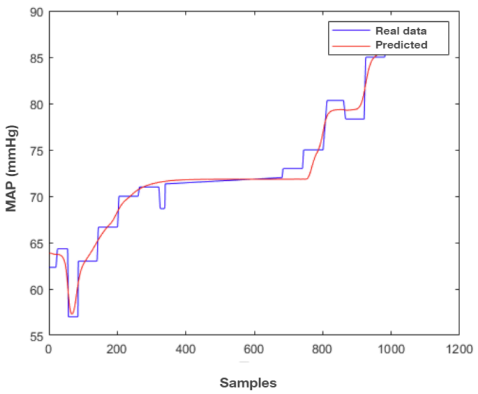

(**d**) Patient 40—Category 4

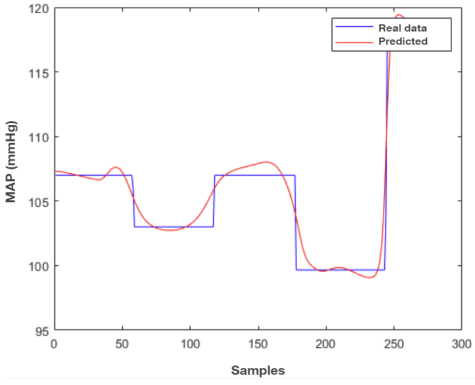

(**e**) Patient 63—Category 5

Figure 5. Results of LSTM-estimated MAP vs. actual MAP values for one patient from each category using the category-specific method.

For categories 4 (moderate correlation) and 5 (strong correlation), the results indicate a very good estimation of MAP using LSTM category-specific methods (Figure 5d,e). This demonstrates the effectiveness of the method in capturing the intricate relationships between drug concentrations and MAP profiles in patients with strong correlations.

3.4. Comparative Study

Figure 6 provides a comparison of the three methods, population-specific, category-specific, and patient-specific, investigated in this paper. The performance metrics employed to assess the obtained results are given in Table 3.

Table 3. Median values for MAE, MSE, and R^2 for different methods.

	Population-Specific	**Category-Specific**	**Patient-Specific**
MAE	0.4139 ± 0.05	0.38115 ± 0.04	0.36325 ± 0.03
MSE	0.332 ± 0.04	0.280 ± 0.03	0.222 ± 0.02
R^2	0.594 ± 0.07	0.606 ± 0.06	0.722 ± 0.05

The maximum MAE is observed for the population-specific method (0.7037), while the minimum is achieved by the patient-specific method (0.1004). The population-specific method reveals the maximum MSE (0.6939), while the minimum is attained by the patient-specific method (0.0256). The minimum R^2 is observed for the population-specific method (0.376), and the maximum is achieved by the patient-specific method (0.872).

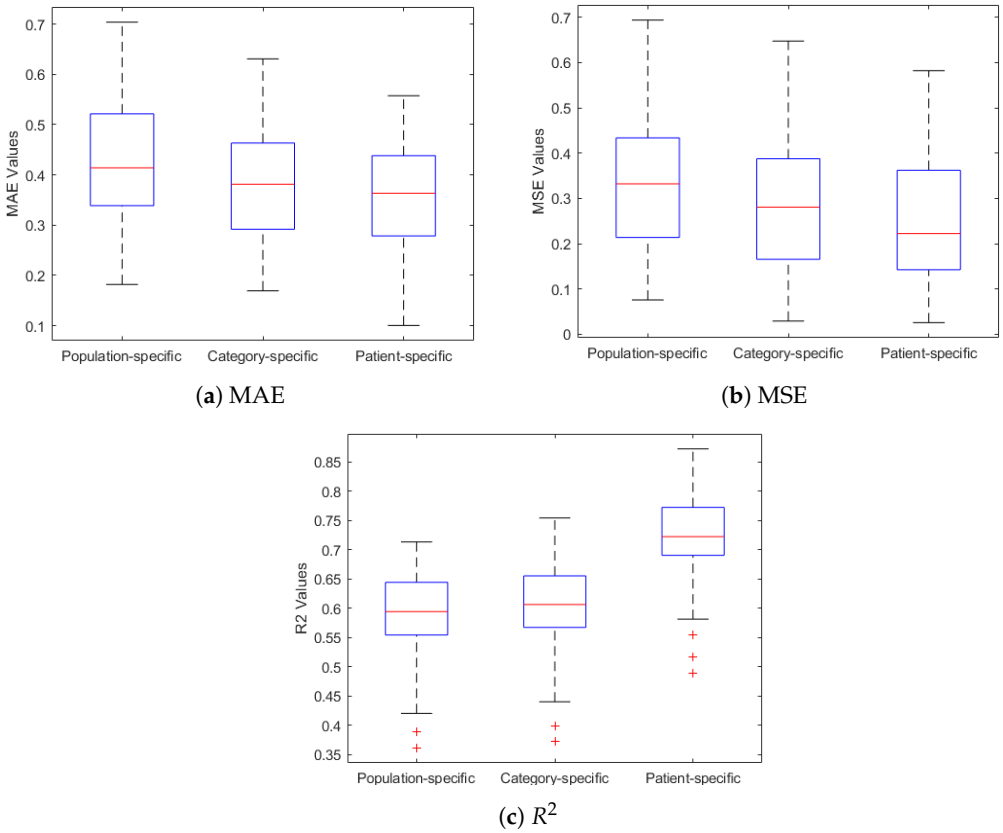

(**a**) MAE (**b**) MSE

(**c**) R^2

Figure 6. Boxplot representation of the performance metrics for each method.

These results indicate that building the LSTM architecture for each patient leads to better predictive performance, as evidenced by lower MAE and MSE, and higher R^2 compared to the population-specific and category-specific methods.

The highly significant p-value of 7.16776×10^{-21} shows that the patient-specific method significantly improves R^2 values, enhancing model estimation capability. Similarly,

the p-values for MSE (0.0125) and MAE (0.0012) also indicate statistically significant differences among the methods, with the patient-specific method resulting in better estimations. The result confirms that the patient-specific method provides the best estimation accuracy; however, due to its intensive nature, this method requires significant computational time. In Table 4, the computational time needed by each method to find the LSTM model architectures is presented.

Table 4. Total time consumed to find the LSTM model architectures for the three methods.

Method	Time Consumed to Find the Architecture
Population-specific	Less than 1 h
Patient-specific	130 h
Category-specific	53 h

In the population-specific method, the selection of the LSTM architecture occurs within an hour, highlighting the efficiency of the method in minimizing time requirements. Conversely, the category-specific method requires 53 h through five runs of the algorithm, each corresponding to a distinct correlation category. The patient-specific method requires significantly higher computation time, i.e., 130 h. The need to iterate individually over 70 patients raises notable concerns, particularly in real-time applications.

The results demonstrate that, while the population-specific method offers a swift convergence to an LSTM architecture (i.e., 1 h), it tends to show higher MAE and MSE values, along with a lower median R^2. The patient-specific methods show the best estimation accuracy; however, the extended computational time needed limits the real-time application of this method. The category-specific method is an intermediary option, effectively balancing computational efficiency (53 h) and individualization.

4. Discussion

In this paper, three distinct methods for selecting the best LSTM model architectures have been investigated for the estimation of MAP during anesthesia: population-specific, patient-specific, and category-specific. The population-specific method employed a uniform architecture for all patients; the patient-specific method fine-tuned the architecture for each individual; and the category-specific method used five distinct architectures based on the correlation categories between inputs (CeProp and CeRemi) and the output (MAP).

The patient-specific method arises as the best architecture, with the lowest MAE and MSE, and the highest R^2. However, this method was also the most computationally intensive, taking 130 h to find the optimal architecture for each patient. The population-specific method was the most computationally efficient (i.g. 1 h). However, it showed the worst estimation accuracy, with the highest MAE and MSE and the lowest R^2. The category-specific method can be seen as a trade-off solution between the patient-specific and population-specific methods, with a computational time of 53 h and an estimation performance close to the patient-specific method. This investigation indicates the pivotal role of architectural selection in deep learning models, as they significantly influence model performance. For LSTM models, these architectural parameters (e.g., the optimizer, the number of layers) had a significant impact on the ability of the model to learn from the data and make accurate estimations. Exploring the best LSTM architectures for MAP estimation has significant implications in clinical settings. By improving the accuracy of MAP forecasting every 5 s, models can enhance individualized patient care, allowing anesthesiologists to make more informed and timely decisions regarding drug administration. This could lead to better maintenance of hemodynamic stability during surgery, reducing the risk of complications such as hypotension or hypertension.

The evaluation of LSTM architecture has been extensively explored in the literature, with various approaches employed to improve predictive performance. Several studies have compared different optimizers, e.g., Adam, SGD, RMSprop, and Adagrad, to deter-

mine their impact on LSTM model performance [30,31]. Other investigations have focused on the selection of activation functions, with sigmoid and tanh functions being widely evaluated [32]. Additionally, research has been conducted on the choice of the number of hidden layers and nodes within each layer, aiming to optimize model complexity and predictive accuracy [33,34]. Previous studies focused on optimizing hyperparameters within a fixed architecture, whereas this study proposes a novel method that tailors the architecture to individual patients and input–output correlation categories. Our finding also highlights the significant effect of the correlation between inputs (CeProp and CeRemi) and the output (MAP) on LSTM model performance. Patients with a high correlation between inputs and output experienced accurate estimations, contrasting with patients with a low correlation, who showed worse predictive performance among the three methods. This reveals the importance of considering the correlation in implementing AI for prediction purposes. This necessitates the imperative of personalized healthcare in the realm of anesthesia, as responses to anesthetic drugs can differ significantly from one individual to another.

While the category-based method offers a practical balance by reducing computational time to 53 h, this computational time is still excessive in a TIVA environment, where a daily routine surgery takes between 20 min and 3 h. To assess the real-time applicability of this approach, the focus was on the last category (patients with the highest correlation between inputs and output). The LSTM model was trained on patients in the last category, excluding one patient (Patient 70), to retain unseen data for testing. A simulated real-life scenario was implemented in MATLAB®, where the trained LSTM received input data (CeProp and CeRemi) and estimated the corresponding MAP every 5 s. These estimations were then compared against the real MAP values. This analysis aims to demonstrate the practical utility of the category-based approach in real-life scenarios.

Figure 7a shows the estimations from both the category-specific (red) and population-specific models (green) against the actual MAP values (blue). It can be observed that the category-specific method provides better estimation than the population-specific method. Figure 7b indicates that the category-specific model's estimations have a distribution closer to the actual MAP values (p-value = 0.0021), hence capturing better the central tendency and variability in the actual MAP values, leading to more accurate estimations. Despite requiring 53 h for the initial architecture selection and model training, the simulation of real-life scenarios provided feasible and accurate MAP estimations. These results are shown in Figure 7. Despite the lengthy initial computational time, its online estimations are accurate, making it an effective approach for MAP estimation. The simulator proposed in [35] can be used to generate additional data and test the proposed solution before applying it on real data.

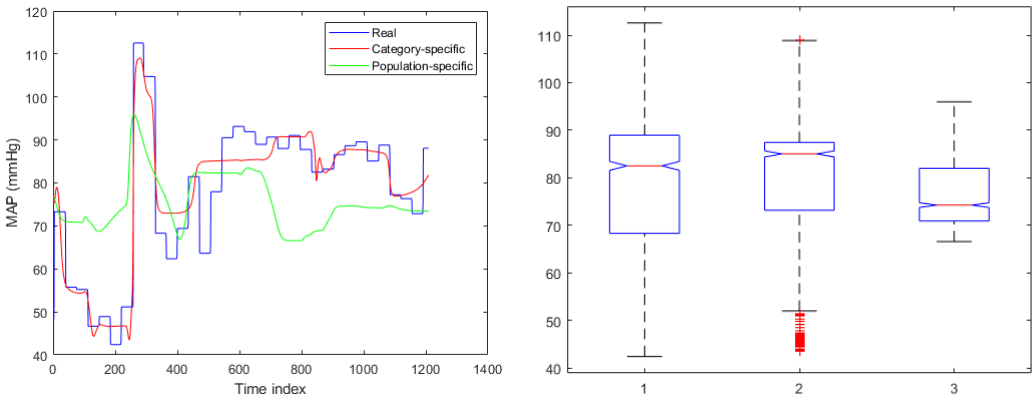

(**a**) (**b**)

Figure 7. Results of an online real-life simulation to estimate the MAP values every 5 s of Patient 70. (**a**) LSTM-estimated MAP using the category-specific method using the population-specific method vs. actual MAP values. (**b**) Boxplot representation of real MAP (1), category-specific model estimation (2), and population-specific model estimation (3).

To determine the feasibility of using the LSTM model for MAP estimation, an initial assessment of the correlations between CeProp, CeRemi, and MAP is essential. Recording CeProp and CeRemi signals for at least 10 min, which corresponds to the duration from the start of infusion of Remifentanil and Propofol until the start of the incision (including intubation and patient preparation), provides a reliable estimate of the correlation. If the correlation coefficient exceeds 0.4, proceed with the LSTM algorithm for accurate estimation. If below 0.4, estimation may not be feasible, and alternative methods should be considered. This ensures the model is used effectively when a strong input–output relationship is present.

Limitations:

- The current study method provides estimation, not forecasting, which means it estimates the MAP value at a particular moment rather than forecasting future values. Although the proposed method offers the advantage of having MAP data that can be sampled as desired, the method could be improved in future research to forecast MAP within a precise prediction horizon. Forecasting MAP values can significantly enhance monitoring capabilities and early warning systems for adverse events. By predicting MAP values, it is possible to enable early detection of potential issues such as hypotension (low blood pressure) [36] and hypertension (high blood pressure) [37], allowing timely interventions to prevent complications. This predictive approach improves patient outcomes by providing healthcare professionals with advanced notice of potential adverse events, facilitating prompt and appropriate responses.
- This approach needs an offline process at the start of a TIVA trial to categorize patients based on their correlation and to identify the best model architecture for each category. Investigating the factors underlying these correlations could improve this approach. Factors such as the medical history of the patient (e.g., heart disease), biometric data (e.g., weight, age, sex), and the type of surgery may all influence the correlation between anesthetic drug concentrations (Propofol/Remifentanil) and MAP. Understanding these factors could facilitate the development of a more efficient categorization process. In our database, patients are categorized into four groups to examine the influence of BMI on the average correlations between the inputs (CeRemi and CeProp) and the output MAP.
  In Table 5, the number of patients found in each BMI category is shown. The figure below illustrates the distribution of average correlations between MAP and the inputs (CeRemi and CeProp) across different BMI categories.

Table 5. Distribution of patients across different BMI categories.

BMI Category	BMI Range	Number of Patients
Underweight	<18.5	3
Normal weight	18.5–24.9	31
Overweight	25–29.9	24
Obesity	≥30	12

The boxplot in Figure 8 shows a significant difference (p-value = 0.0233) in the average correlation based on BMI categories. This indicates that BMI significantly affects the correlation between drug concentrations and MAP. This finding suggests that BMI can be a factor used in the development of a more efficient categorization process.

- The dataset used in this paper consists of a relatively small sample size of 70 patients from a single population, recognizing the non-generalizability of our approach, which relies on a single database. Future research should expand upon these findings, exploring alternative deep learning models, e.g., feed-forward neural networks (FFNs) and recurrent neural networks (RNNs).

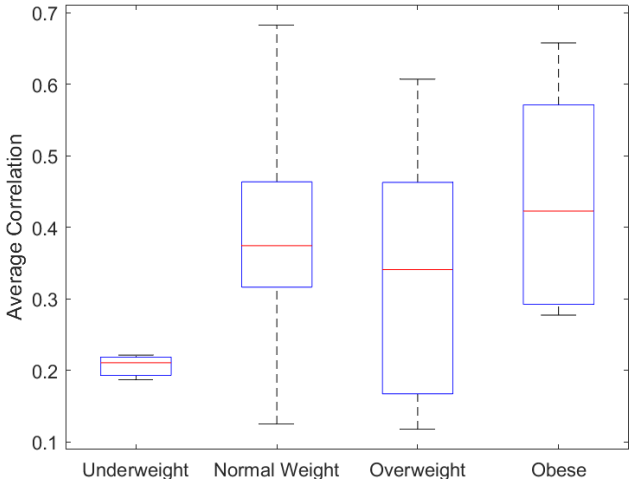

Figure 8. Boxplot representing the distribution of average correlation between MAP and CeRemi and CeProp across different BMI categories.

5. Conclusions

This work proposes a novel approach to find the optimal architecture of the LSTM model for MAP estimation during anesthesia. The results indicate that the patient-specific method is the most accurate but also the most computationally intensive. The population-specific method is the least accurate but also the most computationally efficient. The category-specific method is a trade-off between the two methods. Additionally, the results show that the correlation between the input and the output is an important factor to consider when using AI for estimation. The results highlight the potential use of this optimal LSTM model in clinical practice to enhance personalized anesthesia care.

Author Contributions: Conceptualization G.B.O.; methodology, G.B.O., C.M.I., D.C. and E.Y.; software, G.B.O., E.Y., C.M.I. and D.C.; validation, all authors; formal analysis, G.B.O., C.M.I., E.Y. and D.C.; investigation, G.B.O. and M.N.; resources, M.N., D.C. and C.M.I.; data curation, D.C. and M.N.; writing—original draft preparation, D.C., G.B.O. and E.Y.; writing—review and editing, all authors; visualization, D.C., M.N. and E.Y.; supervision, C.M.I., M.N. and D.C.; project administration, C.M.I.; funding acquisition, C.M.I. All authors have read and agreed to the published version of the manuscript.

Funding: This work received partial funding from Ghent University's special research fund, project number 01j01619. D. Copot acknowledges the support of Flanders Research Foundation, Postdoc grant 12X6823N, 2022-2025.

Institutional Review Board Statement: The study was conducted with the approval of the Ethics Committee of Ghent University Hospital(EC/BC-08020, approved on 20 August 2020).

Informed Consent Statement: Informed consent was obtained from all subjects involved in the study.

Data Availability Statement: Data is contained within the article.

Conflicts of Interest: The authors declare no conflicts of interest.

Appendix A. LSTM Model for MAP Prediction

The LSTM model operates on the training dataset of the inputs (CeProp and CeRemi) $\{x_t\}$ and the output (MAP) $\{y_t\}$, with t denoting time steps. The LSTM model consists of the following layers:

1. *Sequence input layer*: This layer accepts the input data and initializes the sequence for LSTM processing. Each time step t passes the feature vector x_t to the subsequent layers.

2. *LSTM layer*: the model's core, the LSTM layer, operates with mathematical equations. It maintains internal variables, including the following:

- Input gate (i_t): The input gate controls the flow of new information into the cell state. It is computed using the sigmoid activation function σ and is defined as follows:

$$i_t = \sigma(W_{xi}x_t + W_{hi}h_{t-1} + b_i). \quad \text{(A1)}$$

- Forget gate (f_t): The forget gate controls the retention of past information in the cell state and acts as a weighting factor of past-to-new data. It is computed similarly to the input gate and is defined as follows:

$$f_t = \sigma(W_{xf}x_t + W_{hf}h_{t-1} + b_f). \quad \text{(A2)}$$

- Candidate cell state ($\tilde{C}_t$): The candidate cell state represents the new information that could be stored in the cell state. It is computed using the hyperbolic tangent activation function, defined as follows:

$$\tilde{C}_t = \tanh(W_{xc}x_t + W_{hc}h_{t-1} + b_c). \quad \text{(A3)}$$

- Cell state update (C_t): The cell state C_t is updated by combining the previous cell state C_{t-1} with the new information from the input gate and candidate cell state:

$$C_t = f_t \cdot C_{t-1} + i_t \cdot \tilde{C}_t. \quad \text{(A4)}$$

- Output gate (o_t): The output gate controls what information from the cell state should be used to compute the output. It is defined as follows:

$$o_t = \sigma(W_{xo}x_t + W_{ho}h_{t-1} + b_o). \quad \text{(A5)}$$

Here, σ represents the sigmoid activation function, tanh is the hyperbolic tangent activation function, W are weight matrices, b are bias vectors, and h_{t-1} is the previous hidden state.

3. *Fully Connected Layer*: Following the LSTM layer, the Fully Connected Layer prepares the data for classification. It applies learned weights and biases to the output of LSTM.

4. *Regression Layer*: The final Regression Layer assigns a continuous MAP value to each time step, ensuring accurate prediction.

Appendix B. Patient Database

For the database of 70 patients, the clinical investigation involving human subjects was compliant with the regulatory framework stated in the European Regulation (EU) 2017/745. This academic clinical investigation was approved by the Ethics Committee of Ghent University Hospital,the Federal Agency for Medicines, and Health Products of Belgium FAGG (EC/BC-08020, FAGG/80M0840, EudraCT: CIV-BE-20-07-0342442020, clinicaltrials.gov: NCT04986163, principal investigator: Martine Neckebroek).

Table A1. Representative 70-Patient Database Biometric Values (1/2).

Index	Gender	Age (Years)	Height (cm)	Weight (kg)	BMI (kg/m^2)
1	F	31	163	49	18.4
2	F	44	168	57	20.2
3	F	42	168	70	24.8
4	F	71	158	69	27.6
5	F	38	182	87.6	26.4
6	F	41	175	135	44.1
7	F	68	172	67	22.6
8	M	59	183	76	22.7
9	M	50	186	96	27.7
10	M	73	181	83	25.3
11	X	22	165	87	32
12	M	29	183	92	27.5
13	F	54	160	48	18.8
14	X	19	168.7	59	20.7
15	X	26	155	61	25.4
16	F	54	163	58	21.8

Table A1. *Cont.*

Index	Gender	Age (Years)	Height (cm)	Weight (kg)	BMI (kg/m^2)
17	F	50	174	64	21.1
18	F	30	176	74	23.9
19	F	57	164	70	26
20	X	33	162	80	30.5
21	F	62	168	88	31.2
22	F	48	155	56	23.3
23	M	62	183	85	25.4
24	F	36	168	63	22.3
25	M	58	179	94	29.3
26	F	65	162	87	33.2
27	F	49	167	86	30.8
28	M	46	187	97	27.7
29	M	68	176	85	27.4
30	F	50	167	70	25.1
31	M	54	175	90	29.4
32	F	64	164	96	35.7
33	F	46	170	82	28.4
34	F	58	157	53.5	21.7
35	F	41	167	65	23.3

Table A2. Representative 70-Patient Database Biometric Values (2/2).

Index	Gender	Age (Years)	Height (cm)	Weight (kg)	BMI (kg/m^2)
36	F	40	159	63	24.9
37	F	30	160	53	20.7
38	F	18	163	64	24.1
39	F	64	158	58	23.2
40	M	63	171	104	35.6
41	F	30	156	44	18.1
42	F	19	168	54	19.1
43	F	51	168	58	20.5
44	F	59	171	75	25.6
45	M	73	174	67	22.1
46	M	23	173	66	22.1
47	M	25	181	74.5	22.7
48	M	31	170	85	29.4
49	M	32	186	100	28.9
50	F	40	157	85	34.5
51	F	27	157	58	23.5
52	F	71	174	71	23.5
53	M	32	180	78	24.1
54	F	21	166	63	22.9
55	X	48	170	84	29.1
56	M	63	168	82	29.1
57	M	71	175	66	21.6
58	F	48	165	76	27.9
59	F	71	167	83	29.8
60	X	21	160	60	23.4
61	X	21	171	73	25
62	X	34	172	90	30.4
63	X	26	170	50	17.3
64	F	33	172	94	31.8
65	X	22	172	69	23.3
66	F	70	165	62	22.8
67	X	21	168	56	19.8
68	F	35	160	82	32
69	X	21	165	70	25.7
70	X	20	155	49	20.4

Appendix C. MAP Variability among Different Patients and the Safety Intervals

The boxplot in Figure A1 illustrates the distribution of MAP values for each patient, highlighting the variability in MAP measurements.

The observed differences in MAP values among different patients can be attributed to several factors, including individual physiological differences, varying responses to anesthesia, and underlying medical conditions. Some patients exhibit wider variability in their MAP measurements, as shown by the larger distribution. Based on this variability, it is evident that forecasting the MAP every 5 s during surgery is crucial. The situation where the MAP exceeds the safety limits (65–75 mmHg), highlighted in green in the figure, underscores the need for real-time forecasting of the MAP. This paper marks the initial step toward a real-time, online forecasting procedure using AI tools. Future work will focus on developing an algorithm for forecasting MAP and detecting when it exceeds the safety limits, thereby significantly reducing the risks associated with these exceedances.

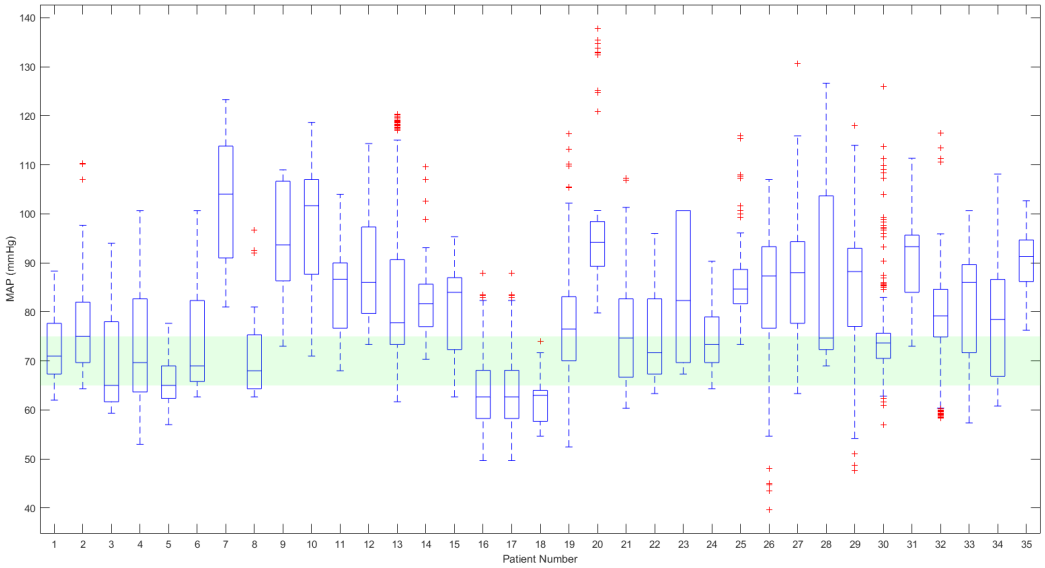

(**a**) From patient 1 to patient 35

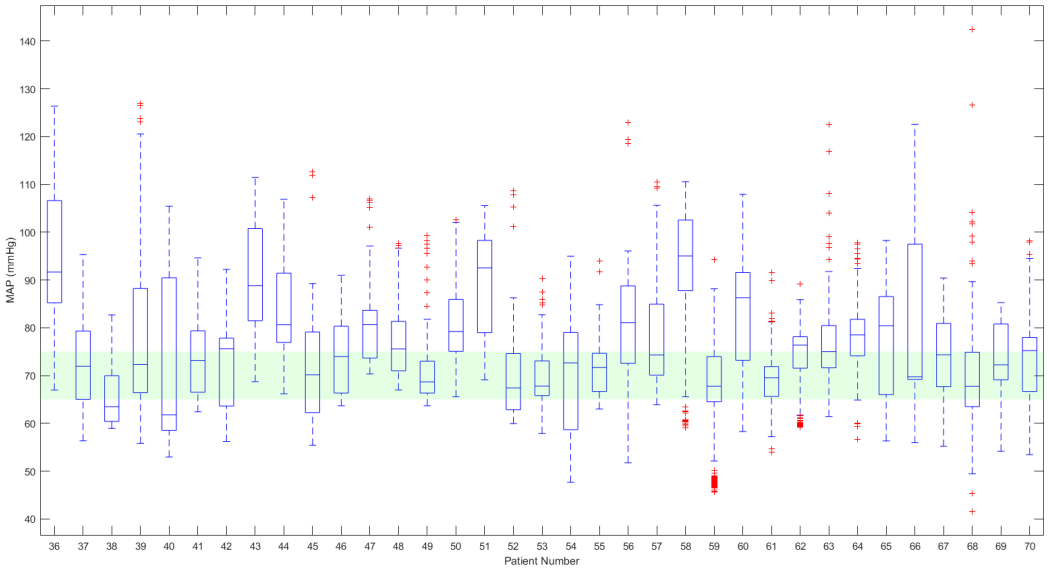

(**b**) From patient 36 to patient 70

Figure A1. Distribution of MAP values across 70 patients. The green shaded area represents the safety interval for MAP (65–75 mmHg) during general anesthesia [38].

References

1. Hino, H.; Matsuura, T.; Kihara, Y.; Tsujikawa, S.; Mori, T.; Nishikawa, K. Comparison between hemodynamic effects of propofol and thiopental during general anesthesia induction with remifentanil infusion: A double-blind, age-stratified, randomized study. *J. Anesth.* **2019**, *33*, 509–515. [CrossRef]

2. Menacho, S.T.; Floyd, C. Current practices and goals for mean arterial pressure and spinal cord perfusion pressure in acute traumatic spinal cord injury: Defining the gaps in knowledge. *J. Spinal Cord Med.* **2021**, *44*, 350–356. [CrossRef] [PubMed]
3. Cava, C.; Salvatore, C.; Castiglioni, I. Pan-cancer classification of gene expression data based on artificial neural network model. *Appl. Sci.* **2023**, *13*, 7355. [CrossRef]
4. Zhang, C.; Zhang, L.; Tian, Y.; Bao, B.; Li, D. A machine-learning-algorithm-assisted intelligent system for real-time wireless respiratory monitoring. *Appl. Sci.* **2023**, *13*, 3885. [CrossRef]
5. De Grauwe, T.; Ghita, M.; Copot, D.; Ionescu, C.M.; Neckebroek, M. Artificial intelligence for pain classification with the non-invasive pain monitor Anspec-Pro. *Acta Anaesthesiol. Belg.* **2022**, *73*, 45–52. [CrossRef]
6. Shamshirband, S.; Fathi, M.; Dehzangi, A.; Chronopoulos, A.T.; Alinejad-Rokny, H. A review on deep learning approaches in healthcare systems: Taxonomies, challenges, and open issues. *J. Biomed. Inform.* **2021**, *113*, 103627. [CrossRef] [PubMed]
7. Xu, Y.; Lu, X.; Cetiner, B.; Taciroglu, E. Real-time regional seismic damage assessment framework based on long short-term memory neural network. *Comput.-Aided Civ. Infrastruct. Eng.* **2021**, *36*, 504–521. [CrossRef]
8. Shah, S.Y.; Yuan, Z.; Lu, S.; Zerfos, P. Dependency analysis of cloud applications for performance monitoring using recurrent neural networks. In Proceedings of the 2017 IEEE International Conference on Big Data (Big Data), Boston, MA, USA, 11–14 December 2017; IEEE: Piscataway, NJ, USA, 2017; pp. 1534–1543.
9. Hewamalage, H.; Bergmeir, C.; Bandara, K. Recurrent neural networks for time series forecasting: Current status and future directions. *Int. J. Forecast.* **2021**, *37*, 388–427. [CrossRef]
10. Ionescu, C.M.; Keyser, R.D.; Copot, D.; Yumuk, E.; Ynineb, A.; Othman, G.B.; Neckebroek, M. Model Extraction From Clinical Data Subject to Large Uncertainties and Poor Identifiability. *IEEE Control Syst. Lett.* **2024**, 1. [CrossRef]
11. Pham, T.D. Time–frequency time–space LSTM for robust classification of physiological signals. *Sci. Rep.* **2021**, *11*, 6936. [CrossRef]
12. Heynen, J.; Copot, D.; Ghita, M.; Ionescu, C.M. Using convolutional neural network online estimators for predicting pain-level variability enables predictive control of anesthesia. In Proceedings of the 2021 25th International Conference on System Theory, Control and Computing (ICSTCC), Iași, Romania, 20–23 October 2021; IEEE: Piscataway, NJ, USA, 2021; pp. 194–199.
13. Gundu, V.; Simon, S.P. PSO–LSTM for short term forecast of heterogeneous time series electricity price signals. *J. Ambient Intell. Humaniz. Comput.* **2021**, *12*, 2375–2385. [CrossRef]
14. Khorram, A.; Khalooei, M.; Rezghi, M. End-to-end CNN+ LSTM deep learning approach for bearing fault diagnosis. *Appl. Intell.* **2021**, *51*, 736–751. [CrossRef]
15. Schnider, T.W.; Minto, C.F.; Gambus, P.L.; Andresen, C.; Goodale, D.B.; Shafer, S.L.; Youngs, E.J. The influence of method of administration and covariates on the pharmacokinetics of propofol in adult volunteers. *J. Am. Soc. Anesthesiol.* **1998**, *88*, 1170–1182. [CrossRef]
16. Minto, C.F.; Schnider, T.W.; Egan, T.D.; Youngs, E.; Lemmens, H.J.; Gambus, P.L.; Billard, V.; Hoke, J.F.; Moore, K.H.; Hermann, D.J.; et al. Influence of age and gender on the pharmacokinetics and pharmacodynamics of remifentanil: I. Model development. *J. Am. Soc. Anesthesiol.* **1997**, *86*, 10–23. [CrossRef]
17. Karnika, S. ISO 14155: Clinical Investigation of Medical Devices for Human Subjects. In *Medical Device Guidelines and Regulations Handbook*; Springer: Berlin/Heidelberg, Germany, 2022; pp. 1–18.
18. Global, S.P.; Windisch, F.; Zimmermann, N.; Knoll, V.; Christodoulou, M.; Habimana, K.; Piccoli, G.; Del Prete, M. *Study on the Implementation of Article 17 of Regulation (EU) 2017/745 on Medical Devices on the EU Market*; European Union: Brussels, Belgium, **2024**.
19. Ionescu, C.M.; Copot, D.; Yumuk, E.; De Keyser, R.; Muresan, C.; Birs, I.R.; Ben Othman, G.; Farbakhsh, H.; Ynineb, A.R.; Neckebroek, M. Development, Validation, and Comparison of a Novel Nociception/Anti-Nociception Monitor against Two Commercial Monitors in General Anesthesia. *Sensors* **2024**, *24*, 2031. [CrossRef] [PubMed]
20. Ahmed, I.; Ahmad, M.; Chehri, A.; Jeon, G. A heterogeneous network embedded medicine recommendation system based on LSTM. *Future Gener. Comput. Syst.* **2023**, *149*, 1–11. [CrossRef]
21. Kaushik, S.; Choudhury, A.; Sheron, P.K.; Dasgupta, N.; Natarajan, S.; Pickett, L.A.; Dutt, V. AI in healthcare: Time-series forecasting using statistical, neural, and ensemble architectures. *Front. Big Data* **2020**, *3*, 4. [CrossRef] [PubMed]
22. Goodfellow, I.; Bengio, Y.; Courville, A. *Deep Learning*; MIT Press: Cambridge, MA, USA, 2016.
23. Smagulova, K.; James, A.P. A survey on LSTM memristive neural network architectures and applications. *Eur. Phys. J. Spec. Top.* **2019**, *228*, 2313–2324. [CrossRef]
24. Mohamed, M.A.; Hassan, H.A.; Essai, M.H.; Esmaiel, H.; Mubarak, A.S.; Omer, O.A. Modified gate activation functions of Bi-LSTM-based SC-FDMA channel equalization. *J. Electr. Eng.* **2023**, *74*, 256–266. [CrossRef]
25. Nagabushanam, P.; Thomas George, S.; Radha, S. EEG signal classification using LSTM and improved neural network algorithms. *Soft Comput.* **2020**, *24*, 9981–10003. [CrossRef]
26. Yu, Y.; Si, X.; Hu, C.; Zhang, J. A review of recurrent neural networks: LSTM cells and network architectures. *Neural Comput.* **2019**, *31*, 1235–1270. [CrossRef] [PubMed]
27. Beale, M.H.; Hagan, M.T.; Demuth, H.B. *Deep Learning Toolbox*; User's Guide; The MathWorks, Inc.: Natick, MA, USA, 2018.
28. Jin, G.; Yi, X.; Zhang, L.; Zhang, L.; Schewe, S.; Huang, X. How does weight correlation affect generalisation ability of deep neural networks? *Adv. Neural Inf. Process. Syst.* **2020**, *33*, 21346–21356.
29. Chen, J.; Liu, Z.; Yin, Z.; Liu, X.; Li, X.; Yin, L.; Zheng, W. Predict the effect of meteorological factors on haze using BP neural network. *Urban Clim.* **2023**, *51*, 101630. [CrossRef]

30. Sharma, J.; Soni, S.; Paliwal, P.; Saboor, S.; Chaurasiya, P.K.; Sharifpur, M.; Khalilpoor, N.; Afzal, A. A novel long-term solar photovoltaic power forecasting approach using LSTM with Nadam optimizer: A case study of India. *Energy Sci. Eng.* **2022**, *10*, 2909–2929. [CrossRef]
31. Chang, Z.; Zhang, Y.; Chen, W. Effective adam-optimized LSTM neural network for electricity price forecasting. In Proceedings of the 2018 IEEE 9th International Conference on Software Engineering and Service Science (ICSESS), Beijing, China, 23–25 November 2018; IEEE: Piscataway, NJ, USA, 2018; pp. 245–248.
32. Vijayaprabakaran, K.; Sathiyamurthy, K. Towards activation function search for long short-term model network: A differential evolution based approach. *J. King Saud Univ.-Comput. Inf. Sci.* **2022**, *34*, 2637–2650.
33. Salman, A.G.; Heryadi, Y.; Abdurahman, E.; Suparta, W. Single layer & multi-layer long short-term memory (LSTM) model with intermediate variables for weather forecasting. *Procedia Comput. Sci.* **2018**, *135*, 89–98.
34. Abbasimehr, H.; Shabani, M.; Yousefi, M. An optimized model using LSTM network for demand forecasting. *Comput. Ind. Eng.* **2020**, *143*, 106435. [CrossRef]
35. Ionescu, C.M.; Neckebroek, M.; Ghita, M.; Copot, D. An Open source patient simulator for design and evaluation of computer based multiple drug dosing control for anesthetic and hemodynamic variables. *IEEE Access* **2021**, *9*, 8680–8694. [CrossRef]
36. Frassanito, L.; Sonnino, C.; Piersanti, A.; Zanfini, B.A.; Catarci, S.; Giuri, P.P.; Scorzoni, M.; Gonnella, G.L.; Antonelli, M.; Draisci, G. Performance of the hypotension prediction index with noninvasive arterial pressure waveforms in awake cesarean delivery patients under spinal anesthesia. *Anesth. Analg.* **2022**, *134*, 633–643. [CrossRef]
37. Kandil, H.; Soliman, A.; Alghamdi, N.S.; Jennings, J.R.; El-Baz, A. Using mean arterial pressure in hypertension diagnosis versus using either systolic or diastolic blood pressure measurements. *Biomedicines* **2023**, *11*, 849. [CrossRef]
38. Khanna, A.K.; Kinoshita, T.; Natarajan, A.; Schwager, E.; Linn, D.D.; Dong, J.; Ghosh, E.; Vicario, F.; Maheshwari, K. Association of systolic, diastolic, mean, and pulse pressure with morbidity and mortality in septic ICU patients: A nationwide observational study. *Ann. Intensive Care* **2023**, *13*, 9. [CrossRef] [PubMed]